



# Pd<sub>17</sub>Se<sub>15</sub>-Pd<sub>3</sub>B nanocoral electrocatalyst for selective oxygen reduction to hydrogen peroxide in near-neutral electrolyte

Juyeon Lee<sup>a,1</sup>, Seung Woo Choi<sup>a,1</sup>, Seoin Back<sup>b</sup>, Hongje Jang<sup>a,\*</sup>, Young Jin Sa<sup>a,\*</sup>

<sup>a</sup> Department of Chemistry, Kwangju University, Seoul 01897, Republic of Korea

<sup>b</sup> Department of Chemical and Biomolecular Engineering, Institute of Emergent Materials, Sogang University, Seoul 04107, Republic of Korea

## ARTICLE INFO

### Keywords:

H<sub>2</sub>O<sub>2</sub> electrosynthesis  
Electrocatalyst  
Oxygen reduction reaction  
Pd<sub>17</sub>Se<sub>15</sub>  
Pd<sub>3</sub>B

## ABSTRACT

An efficient approach to shift the reaction pathway from the 4-electron oxygen reduction reaction (4e<sup>-</sup> ORR) to the 2e<sup>-</sup> ORR is by fabricating precious metal compounds. The selectivity of the latter reaction is critical for the efficiency of H<sub>2</sub>O<sub>2</sub> electrosynthesis technology. Herein, we demonstrate the high 2e<sup>-</sup> ORR activity and selectivity of a nanocoral-shaped Pd-based compound comprising Pd<sub>17</sub>Se<sub>15</sub> and Pd<sub>3</sub>B mixed phases (Pd-Se-B NC). In contrast, metallic Pd exhibited nearly 100% 4e<sup>-</sup> ORR selectivity. The mass activity of Pd-Se-B NC for H<sub>2</sub>O<sub>2</sub> generation was ~37-fold higher than that of the Pd black catalyst. Importantly, Pd-Se-B NC exhibited one of the highest H<sub>2</sub>O<sub>2</sub> electrosynthesis activities in neutral media reported to date. The chemical states and composition of the Pd-Se-B NC remained almost intact even after sustained electrocatalysis.

## 1. Introduction

Hydrogen peroxide is one of the most important chemicals used as a green oxidant in many industries, including pulp processing, disinfection, and wastewater treatment [1]. The anthraquinone process for producing H<sub>2</sub>O<sub>2</sub> has supplied the majority of the global demand. However, the issues of the traditional process, including the high energy consumption and organic waste generation, necessitate alternative processes for H<sub>2</sub>O<sub>2</sub> production. The electrochemical H<sub>2</sub>O<sub>2</sub> synthesis has been demonstrated as a promising approach because of its environmental benignity and integrability with renewable energy sources. The electrosynthesis of H<sub>2</sub>O<sub>2</sub> can be achieved via the two-electron oxygen reduction reaction (2e<sup>-</sup> ORR: O<sub>2</sub> + 2H<sup>+</sup> + 2e<sup>-</sup> → H<sub>2</sub>O<sub>2</sub>). However, this reaction competes with the 4e<sup>-</sup> ORR (O<sub>2</sub> + 4H<sup>+</sup> + 4e<sup>-</sup> → 2H<sub>2</sub>O), which is thermodynamically more exergonic than the 2e<sup>-</sup> ORR. In addition, the produced H<sub>2</sub>O<sub>2</sub>, as an unstable compound, is vulnerable to further reduction and chemical decomposition. Therefore, the development of selective electrocatalysts for the 2e<sup>-</sup> ORR is a key task for the practical application of the electrochemical H<sub>2</sub>O<sub>2</sub> production technology [2–6].

Various nanomaterials based on precious metals [7–20], non-precious metals [21–29], and doped carbons [30–39] have been investigated as ORR electrocatalysts. The 2e<sup>-</sup>/4e<sup>-</sup> ORR selectivity was found to be sensitive to the chemical composition and active site

structures. For example, transition metal-nitrogen-carbon composites exhibited high 4e<sup>-</sup> ORR selectivity while N-free atomically dispersed transition metals on carbon materials were selective for the 2e<sup>-</sup> ORR [23,24,28,29]. For metal-free heteroatom-doped carbons, carboxylic, ring ether, quinone oxygen groups, and pyrrolic nitrogen groups have been proposed as the active sites [30,31,35,39]. Despite the recent advances and understanding on the active sites, non-precious metal catalysts and carbon-based materials are still only operable at high pH with low overpotentials while high overpotentials are required in acidic and neutral electrolytes. Because H<sub>2</sub>O<sub>2</sub> decomposition rate is significant at high pH, H<sub>2</sub>O<sub>2</sub> electrosynthesis system efficiently operating in acidic or neutral electrolytes is desirable. At medium to low pH, precious metals such as Pt and Pd show high ORR activity (low overpotential) but the 4e<sup>-</sup> ORR is dominant for these metals; thus, they are suited for use as fuel cell cathodes. The high 4e<sup>-</sup> ORR catalytic abilities of these precious metals are ascribed to their optimal O binding energies and the presence of ensemble sites that enable a facile O=O cleavage, leading to H<sub>2</sub>O production (via the 4e<sup>-</sup> ORR). In this regard, controlling the atomic arrangement of precious metal catalysts absence of ensemble sites can be an effective strategy to achieve a high 2e<sup>-</sup> ORR selectivity. Accordingly, efficient precious metal-based 2e<sup>-</sup> ORR electrocatalysts have been developed by alloying with less catalytically active metals such as Hg, Au, and Pb [7–12]. The secondary metals act as atomic spacers that

\* Corresponding authors.

E-mail addresses: [hjang@kw.ac.kr](mailto:hjang@kw.ac.kr) (H. Jang), [youngjinsa@kw.ac.kr](mailto:youngjinsa@kw.ac.kr) (Y.J. Sa).

<sup>1</sup> These authors contributed equally to this work.

increase the distance between precious metal atoms, thereby removing the ensemble sites and prohibiting the  $4e^-$  ORR [13]. For instance, elimination of Pd–Pd–Pd ensemble sites by alloying with Hg (i.e. formation of Pd–Hg–Pd active motif) changed the  $O_2$  adsorption mode that prohibits O=O breakage. However, due to the toxicities or high costs of the secondary metals, exploration of other precious metal compounds is highly pursued.

It was assumed that there were other metal compounds with such active motifs. In this regard, we previously conducted high-throughput screening and density functional theory (DFT) calculations to discover electrocatalysts from the materials database [13]. As a result, dozens of compounds were found that were predicted to possess high activity, selectivity, and stability for the  $2e^-$  ORR, even better than the state-of-the-art PtHg<sub>4</sub> composition. The candidates include Pd–Hg [9], Pd–Se (this work), Au–Cd (not reported so far).

Herein, motivated by the previous DFT calculation results, a nanocoral-shaped Pd-based electrocatalyst comprising mixed Pd<sub>17</sub>Se<sub>15</sub> and Pd<sub>3</sub>B phases (denoted as Pd–Se–B NC) was synthesised and its catalytic capability for the electrochemical H<sub>2</sub>O<sub>2</sub> production was examined. Pd–Se–B NC exhibited high  $2e^-$  ORR activity and selectivity in a near-neutral electrolyte (pH 8.0), whereas a commercial Pd black catalyst showed nearly exclusive  $4e^-$  ORR selectivity. Nanomaterial with the mixed composition of Pd and nonmetal elements is firstly demonstrated as the  $2e^-$  ORR electrocatalyst while precious metal alloys have been predominantly used. The chemical and compositional stabilities of the Pd–Se–B NC during sustained electrocatalysis are also demonstrated.

## 2. Experimental section

### 2.1. Synthesis of Pd–Se–B nanocoral catalyst

Pd–Se–B NC was synthesized by reducing agent-assisted polyol method. In details, 0.27 mmol of Pd(acac)<sub>2</sub> and 0.03 mmol of H<sub>2</sub>SeO<sub>3</sub> were fully dissolved in 45 mL of triethylene glycol (TEG) in a two-neck round bottom flask. 120 mg of NaBH<sub>4</sub> was added the solution under vigorous stirring. When the color of mixture turned black, the mixture was transferred into pre-heated oil bath at 220 °C and incubated for 3 h. After cooled to room temperature, the resulting products were collected by centrifugation at 9000 rpm for 10 min. The precipitated products were carefully washed with ethanol and DI water several times and dispersed.

### 2.2. Characterization methods

The size and morphology of Pd–Se–B NC were confirmed by energy-filtering transmission electron microscope (TEM, LIBRA 120, Carl Zeiss) and high-resolution field emission scanning electron microscope (SEM, SU8010, Hitachi). High-resolution imaging, high-angle annular dark-field scanning TEM (HAADF-STEM), and energy dispersive X-ray spectroscopy (EDS) mapping were accomplished by Cs-corrected STEM (JEM-ARM200F, JEOL). X-ray diffraction (XRD) pattern was obtained by X-ray diffractometer (SmartLab, Rigaku). UV-Vis spectrum of dispersed Pd–Se–B NC was collected using Lambda-465 (PerkinElmer). For X-ray photoelectron spectroscopy (XPS) measurements, Pd–Se–B NC catalyst ink (described in Section 2) was dropped on a piece of carbon paper. XPS spectra of the catalyst-coated carbon paper were acquired using K-alpha<sup>+</sup> X-ray photoelectron spectrometer (Thermo Fisher Scientific) with monochromated Al K $\alpha$  (1486.6 eV) which was calibrated using C 1s peak for C–C bonding at 284.8 eV. Surface etching in the XPS measurement was performed using a monoatomic Ar<sup>+</sup> plasma at 1 keV. XPS deconvolution was conducted using the XPSPeak41 software. The background of the raw spectra was removed using Shirley-type curve and mixed Gaussian–Lorentzian (70% Gaussian) functions were used for the deconvolution.

### 2.3. Electrochemical characterizations

#### 2.3.1. Preparation of the catalyst film

Before every measurement, a rotating ring disk electrode (RRDE), consisting of glassy carbon (GC) disk with a Pt ring, was polished on a microcloth with 1.0  $\mu$ m and 0.05  $\mu$ m alumina aqueous suspension for 10 min for each and rinsed with DI water. The Pd–Se–B NC catalyst ink was fabricated by mixing 1.0 mL Pd–Se–B NC aqueous dispersion, 16.8  $\mu$ L of 0.5% Nafion solution, and 210  $\mu$ L of anhydrous EtOH, and sonicating in an ultrasonic bath for 20 min. An aliquot (30  $\mu$ L) of the ink was pipetted, dropped onto the GC disk (5.61 mm in diameter) of the RRDE, and dried at RT. For Pd black, 3 mg of Pd black, 50  $\mu$ L of 0.5% Nafion solution, 100  $\mu$ L of DI water, and 1.8 mL of anhydrous EtOH were added into a vial and sonicated for 20 min. An aliquot (16  $\mu$ L) of the ink was pipetted and dropped onto the GC disk and dried at RT. The catalyst loading was controlled to be 0.1 mg<sub>Pd</sub> cm<sup>−2</sup>. RRDE measurement of the bare GC electrode was conducted using the polished RRDE.

#### 2.3.2. Measurements of ORR activity and selectivity using RRDE

A conventional three electrode setup was built for all the RRDE measurements. RRDE was used as a working electrode. Ag/AgCl (RE-5B, BASi, filled with 3 M KCl) for acidic and neutral electrolytes and Hg/HgO (CHI152, CH Instruments, filled with 1 M KOH) for alkaline electrolyte were used as reference electrodes. A graphite rod was used as a counter electrode. Electrochemical tests were conducted using a bipotentiostat (CHI760E, CH Instruments). The catalyst-coated RRDE or bare RRDE was equipped on an electrode rotator (RDE710, Gamry Instruments) and immersed in a desired electrolyte (pH 8.0 0.1 M potassium phosphate (KPi) buffer, pH 7.0 0.1 M KPi, 1 $\times$  phosphate buffer saline (PBS), 0.1 M KOH, or 0.5 M H<sub>2</sub>SO<sub>4</sub>). KPi electrolytes were prepared by mixing 0.1 M KOH and 0.1 M KH<sub>2</sub>PO<sub>4</sub> at a ratio to obtain a desired pH. Electrochemical impedance spectroscopy (EIS) was performed at 0.68 V (vs. reversible hydrogen electrode; RHE) from 100,000 to 1 Hz in O<sub>2</sub>-saturated electrolyte with a potential amplitude of 10 mV. From the Nyquist plot of the EIS spectra, the series resistance ( $R_s$ ) was obtained from the real part impedance at a high frequency region. 90% of the  $R_s$  value was used to correct Ohmic potential drop. The conversion to  $iR$ -corrected potential scale versus RHE was accomplished according to the following equations:

$$E_{\text{RHE}, iR\text{-corrected}} = E_{\text{Ag/AgCl}} + 0.21 + 0.0592 \times \text{pH} - 0.9iR_s$$

$$E_{\text{RHE}, iR\text{-corrected}} = E_{\text{Hg/HgO}} + 0.89 - 0.9iR_s$$

where  $i$  stands for the measured current. The ORR activity and selectivity was measured by linear sweep voltammetry (LSV) from 1.1 to 0.2 V (vs. RHE) in O<sub>2</sub>-saturated electrolyte at a potential scan rate of 5 mV s<sup>−1</sup> while the Pt ring potential was fixed at 1.3 V (vs. RHE). From the LSV results, H<sub>2</sub>O<sub>2</sub> molar selectivity was calculated using the following equation:

$$\text{H}_2\text{O}_2 \text{ molar selectivity (\%)} = \frac{200}{1 + \frac{N \times i_d}{i_r}}$$

where  $N$ ,  $i_d$ , and  $i_r$  stand for the collection efficiency of the RRDE, disk current, and ring current, respectively. The collection efficiency values were experimentally determined using a three-electrode setup composed of polished RRDE, Pt coil, and Ag/AgCl as working, counter, and reference electrodes, respectively, in various electrolytes with 2 mM K<sub>3</sub>[Fe(CN)<sub>6</sub>]. After purging the electrolyte with Ar gas, chronoamperometry was first performed at 0.5 V (vs. Ag/AgCl) with the ring potential held at 0.5 V (vs. Ag/AgCl) with the electrode rotation of 1600 rpm (Fig. S1). No reactions were expected to occur under these conditions and thus the measured ring current can be considered as the background. Then, another chronoamperometry was carried out at −0.3 V (vs. Ag/AgCl) with the ring potential held at 0.5 V (vs. Ag/AgCl). The collection efficiency was calculated by averaging the current ratio

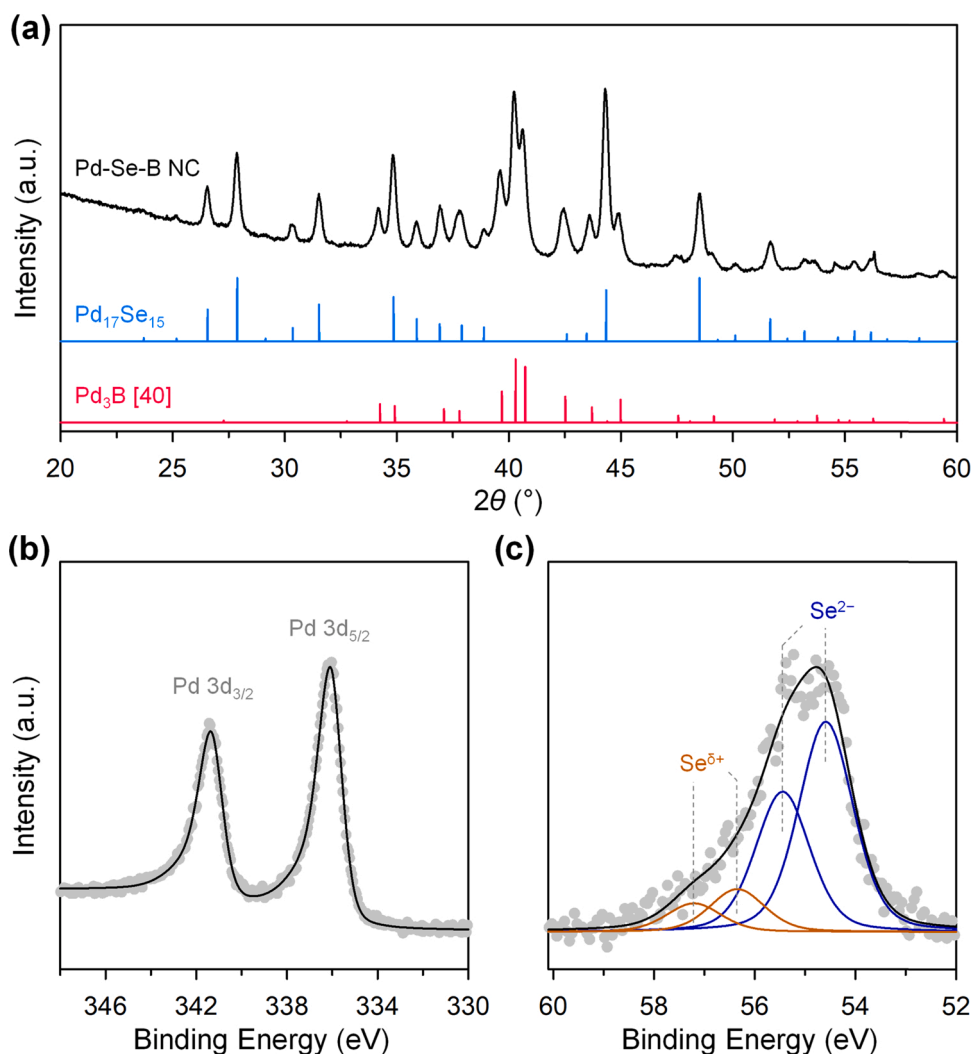


Fig. 1. (a) XRD pattern of Pd-Se-B NC and reference patterns. Deconvoluted (b) Pd 3d and (c) Se 3d XPS spectra of Pd-Se-B NC.

collected at ring and disk in the last 5 s using the following equation:

$$N = \frac{|i_r - i_{r,bg}|}{i_d}$$

where the  $i_{r,bg}$  indicates the background ring current. The resulting values were similar to that provided by the manufacturer (Fig. S1). Cyclic voltammetry (CV) was conducted from 0.05 to 1.1 V (vs. RHE) 5 times at a scan rate  $50 \text{ mV s}^{-1}$  in Ar- or  $\text{N}_2$ -saturated electrolytes.

### 2.3.3. Bulk electrolysis measurement

Capability of Pd-Se-B for sustained  $2e^-$  ORR was tested by bulk electrolysis measurements. For this purpose, a three-electrode setup was built in H-cell configuration, where the catalyst-coated carbon paper, Ag/AgCl, and Pt coil were used as working, reference, and counter electrodes, respectively. In H-cell system, the working electrode was separated from the counter electrode, preventing the oxidation of produced  $\text{H}_2\text{O}_2$  at the counter electrode. Nafion 212 membrane was used to separate the electrolyte chambers. Before use, Nafion 212 membrane was activated by the following steps. First, the membrane was soaked in 1 M  $\text{H}_2\text{SO}_4$  at  $80^\circ\text{C}$  for 1 h, followed by treatment in 3 wt%  $\text{H}_2\text{O}_2$  at  $80^\circ\text{C}$  for 1 h. At the end of each step, the membrane was rinsed with DI water. The treated Nafion was immersed in DI water and maintained at  $80^\circ\text{C}$  for 1 h. After repeating the DI water step once more, the membrane was stored in DI water at room temperature. For the fabrication of the catalyst-coated carbon paper, the above-mentioned Pd-Se-B NC

catalyst ink was deposited on a piece of carbon paper ( $1 \text{ cm} \times 1 \text{ cm}$ , TGP-H-60, Toray) to achieve the catalyst loading of  $0.1 \text{ mg}_{\text{Pd}} \text{ cm}^{-2}$ . Chronoamperometry was performed at a desired applied potential for 1 h in  $\text{O}_2$ -saturated 0.1 M KPi (pH 8.0) electrolyte.

## 3. Results and discussion

### 3.1. Materials characterization

The Pd-Se-B NC catalyst was prepared via the polyol reaction of the Pd(II) and Se(IV) precursors in TEG under the presence of a strong reducing agent ( $\text{NaBH}_4$ ). After establishing a homogeneous precursor solution of  $\text{Pd}(\text{acac})_2$  and  $\text{Na}_2\text{SeO}_3$  in TEG under an inert  $\text{N}_2$  atmosphere,  $\text{NaBH}_4$  was rapidly injected into this solution to initiate the reaction. Nanoseeds formed immediately following the injection, and the solution turned black. The mixture was heated at  $220^\circ\text{C}$  for 3 h to achieve further growth and crystallisation. The resultant Pd-Se-B NC exhibited a uniform and excellent absorption in the ultraviolet, visible, and near-infrared regions (Fig. S2). The crystal phases and crystallinity of the Pd-Se-B NC were identified using XRD. The XRD pattern of Pd-Se-B NC confirms that the sample contains  $\text{Pd}_{17}\text{Se}_{15}$  (JCPDS #29-1437) and  $\text{Pd}_3\text{B}$  [40] crystalline phases (Fig. 1a and S3). Scherrer analysis revealed that the crystallite sizes of  $\text{Pd}_{17}\text{Se}_{15}$  and  $\text{Pd}_3\text{B}$  phases were  $30 \pm 2$  and  $20 \pm 4 \text{ nm}$ , respectively.

The surface chemical states and elemental composition of the Pd-Se-

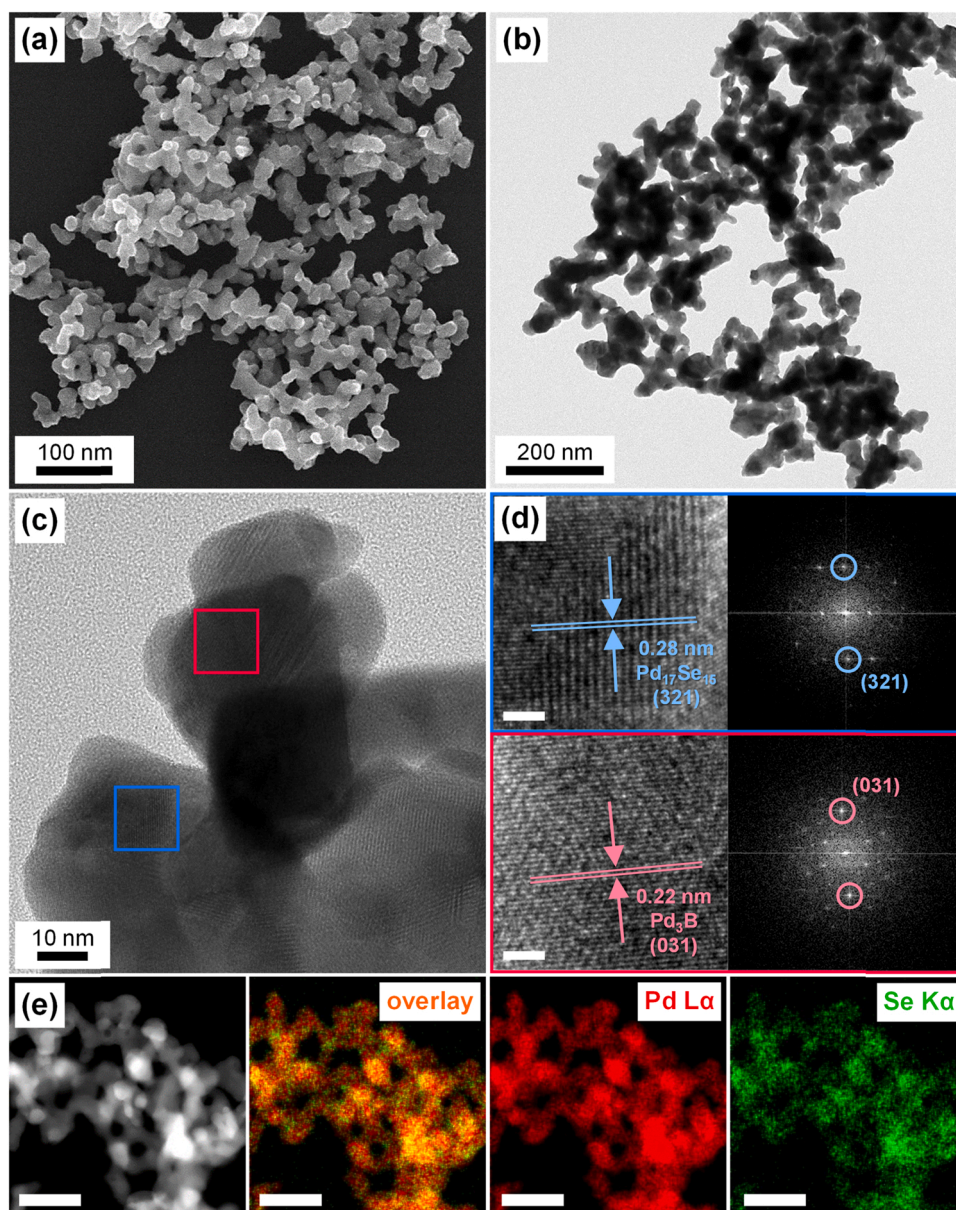


**Fig. 2.** (a) SEM, (b) TEM, and (c) HR-TEM images of Pd-Se-B NC. (d) Magnified HR-TEM images and FFT patterns of the selected areas (indicated by red and blue square lines) of the HR-TEM image shown in (c). (e) HAADF-STEM image and EDS element mapping of Pd-Se-B NC. Scale bars are 2 and 100 nm in (d) and (e), respectively.

B NC were analysed using XPS. The Pd 3d XPS spectrum illustrated in Fig. 1b could be deconvoluted into the peaks of Pd 3d<sub>5/2</sub> (336.1 eV) and Pd 3d<sub>3/2</sub> (341.4 eV). The Pd 3d<sub>5/2</sub> peak position is higher than that of Pd metal (~335.0 eV) but lower than that of PdO (~336.7 eV). The lower Pd 3d<sub>5/2</sub> binding energy compared with that of PdO results from the lower electronegativities of Se and B than that of O. The Pd XPS peaks exhibit a slight asymmetry that can be generally observed in metallic materials; this finding indicates that Pd-Se-B NC possesses metallic properties [41]. The deconvoluted Se 3d XPS spectrum of the Pd-Se-B NC displays major Se<sup>2-</sup> peaks as well as small peaks for the partially oxidised Se<sup>δ+</sup> (Fig. 1c). The presence of B in the sample, however, could not be confirmed because of the inherently low sensitivity of the B 1s XPS peak [42]. The Ar<sup>+</sup>-plasma surface etching on Pd-Se-B NC was performed, and results indicate a significant increase in the ratio of the surface content of Pd relative to that of Se (Pd/Se) (from 0.82 to 1.25). This result suggests that the Se concentration is enriched on the surface of Pd-Se-B NC, thereby indicating the existence of other Pd-based phase

in the inner part of the sample (the Pd<sub>3</sub>B phase). Therefore, the nanocoral frameworks are predominantly composed of the Pd<sub>17</sub>Se<sub>15</sub> phase, which covers Pd<sub>17</sub>Se<sub>15</sub> and Pd<sub>3</sub>B phases at the core. The existence of B in Pd-Se-B NC was verified by inductively coupled plasma optical emission spectrometry, and results indicate that Pd-Se-B NC contains 16.0 at% B, 21.6 at% Se, and 62.4 at% Pd (Table S1).

The morphology and nanostructure of the Pd-Se-B NC were investigated using scanning and transmission electron microscopy (SEM and TEM, respectively). The SEM and TEM images indicate that Pd-Se-B NC possesses a porous nanocoral structure with an overall dimension of a few micrometres consisting of networked protruding nanorods with an approximate average diameter of 20–40 nm, which agrees well with the XRD analysis (Fig. 2a and b). This type of structure can provide a high surface area, which facilitates diffusion and access to the surface catalytic sites. The high-resolution TEM (HR-TEM) image shows that the framework of the nanocoral structure comprises of multiple crystalline grains pointed in various random directions (Fig. 2c). The HR-TEM

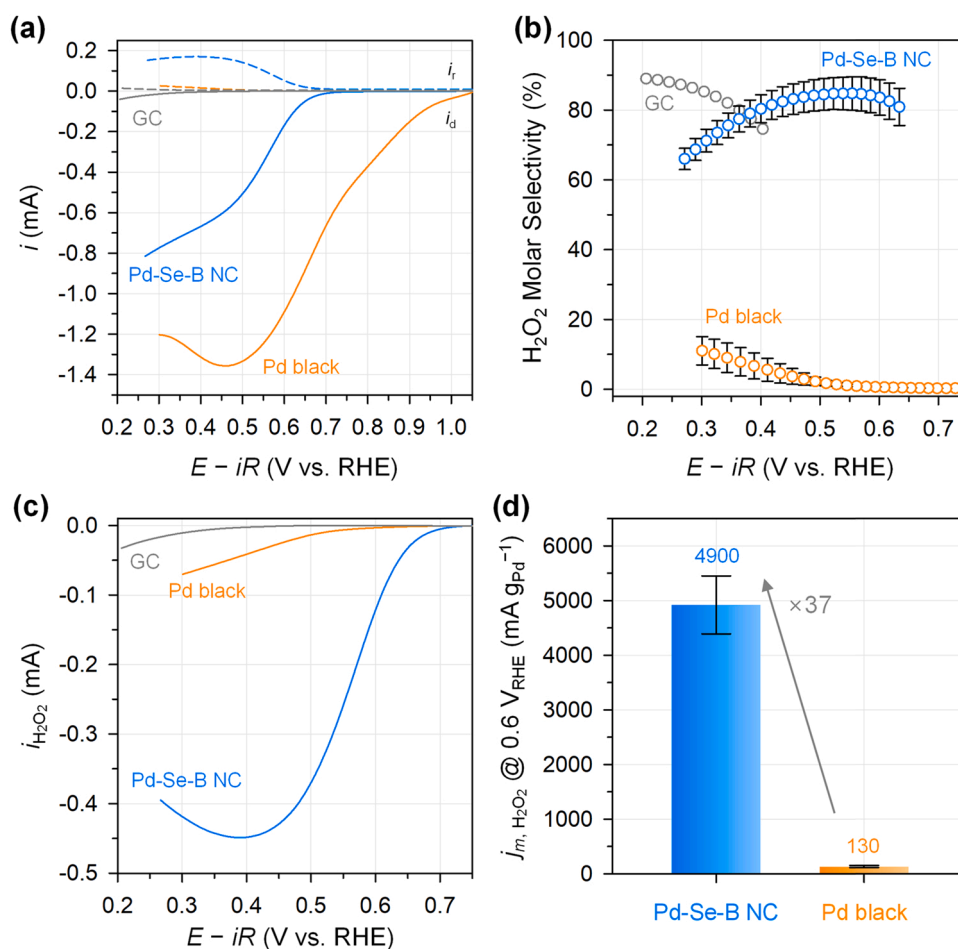


**Fig. 3.** (a) LSV curves of Pd-Se-B NC, Pd black, and glassy carbon (GC) electrode obtained from RRDE measurements in  $O_2$ -saturated KPi buffer (pH 8.0, 0.1 M) with an electrode rotation speed of 1600 rpm and (b) corresponding  $H_2O_2$  molar selectivity. (c)  $H_2O_2$  partial current density Pd-Se-B NC, Pd black, and GC electrode calculated from the ring current in (a). (d) Bar graph depicting the  $H_2O_2$  mass activity per Pd ( $j_{m, H_2O_2}$ ) at 0.6 V (vs. RHE).

image also shows clear lattice fringes. Fast Fourier-transform (FFT) patterns obtained from the selective domains correspond to the (321) plane of the  $Pd_{17}Se_{15}$  and the (031) plane of the  $Pd_3B$  (Fig. 2d and S3). EDS mapping revealed the distribution of Pd and Se (Fig. 2e).

### 3.2. Electrochemical tests

The electrocatalytic activity and selectivity of the Pd-Se-B NC toward the  $2e^-$  ORR were examined using RRDE measurements. The electrocatalytic properties of Pd-Se-B NC were compared with those of Pd black to investigate the effects of the presence of the Pd ensemble sites. LSV curves of the Pd-Se-B NC and Pd black measured in a near-neutral electrolyte, KPi buffer (pH 8.0, 0.1 M), exhibit a marked difference in their onset potentials (Fig. 3a). Pd-Se-B NC exhibits an onset potential of 0.70 V (vs. RHE), which is close to the thermodynamic equilibrium potential of  $2e^-$  ORR, while Pd black displays a more positive onset potential of 1.0 V. The positively shifted onset potential suggests a mechanistic preference for the  $4e^-$  ORR by Pd black since the equilibrium potentials for  $2e^-$  and  $4e^-$  ORR are 0.70 and 1.23 V (vs. RHE), respectively. This was confirmed by the ORR selectivity calculated from the RRDE measurements displayed in Fig. 3b; Pd black exhibits a low  $H_2O_2$  selectivity below 10% over the entire potential range investigated, while Pd-Se-B NC exhibits high  $H_2O_2$  selectivities with a maximum value of  $85 \pm 5\%$ . The  $H_2O_2$  partial current was extracted from the ring current of the LSV data (Fig. 3c). The onset potential for the  $H_2O_2$  generation is 0.70 V (vs. RHE) for Pd-Se-B NC, which is 0.14 V higher than that of Pd black. The mass activity for  $H_2O_2$  generation per Pd of Pd-Se-B

NC is  $4900 \text{ mA g}_{Pd}^{-1}$ , which is 37-fold higher than that of Pd black ( $130 \text{ mA g}_{Pd}^{-1}$ ; Fig. 3d). Pd-Se-B NC exhibits one of the highest  $2e^-$  ORR activities compared to previously reported electrocatalysts in near-neutral media [43–50] (Table S2).

In Pd-Se-B NC, Se and B can have dual roles in controlling the activity and selectivity of Pd active sites. The first effect is the modification of electronic structure of Pd, which is related to O adsorption ability. Pd itself has slightly higher O binding strength compared to the optimum strength [8]. Therefore, weakening the bonding can enhance the activity. This is enabled by alloying with other elements that donate electron density to Pd, that is, elements with lower electronegativity than Pd (lowering  $d$ -band center of Pd). B possesses a slightly lower electronegativity than Pd, so that the adsorption property of Pd can be optimized. In contrast, Se with higher electronegativity than Pd has an opposite effect, which is disadvantageous for the ORR activity. The second effect is the modification of atomic arrangement. In more particular, Se and B atoms can act as “spacer atoms” which leave a space between Pd atoms. This alters  $O_2$  adsorption from side-on to end-on mode, prohibiting  $O=O$  bond breakage and leading to  $2e^-$  reaction pathway. It is assumed that the modified atomic arrangement has more dominant catalytic effect than the electronic effect to tune the ORR selectivity in Pd-Se-B NC compared to metallic Pd. In addition, the nanocoral structure also contribute to high catalytic activity because of its high surface area and facilitated mass transport.

The  $2e^-$  ORR activity of Pd-Se-B NC in a more common electrolyte, PBS, was tested (Fig. S4). Pd-Se-B NC and Pd black show remarkable difference in their onset potentials of 0.7 and 0.9 V (vs. RHE),

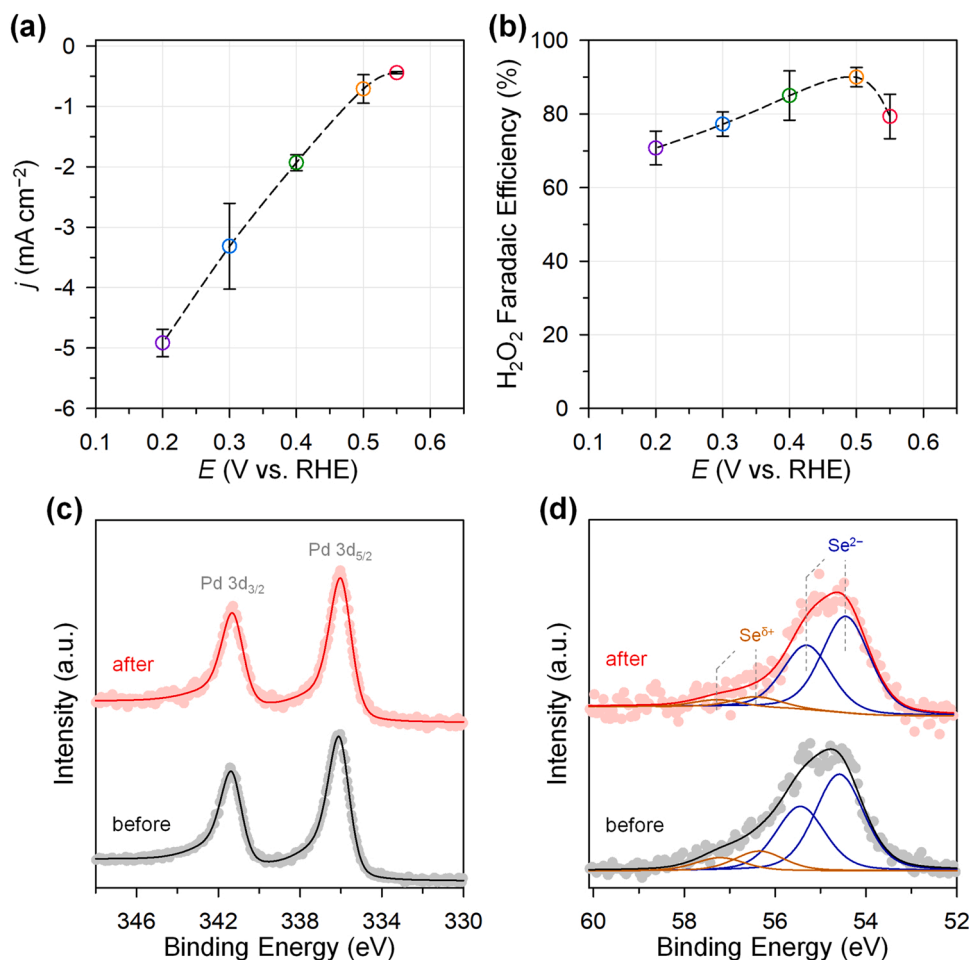


**Fig. 4.** (a) Current density and (b) corresponding H<sub>2</sub>O<sub>2</sub> FE measured using the catalyst-coated carbon paper in an H-cell as a function of the applied potential. (c) Pd 3d and (d) Se 3d deconvoluted XPS spectra of Pd-Se-B NC before and after the bulk electrolysis measurements at 0.3 V (vs. RHE).

respectively (Fig. S4a). The higher onset potential implies the 4e<sup>-</sup> ORR occurring on Pd metal. In addition, higher ring current observed for Pd-Se-B NC indicates its better 2e<sup>-</sup> ORR selectivity than that of Pd black. This was confirmed by H<sub>2</sub>O<sub>2</sub> molar selectivity calculated from the RRDE measurements (Fig. S4b). In the entire potential range, Pd-Se-B NC shows higher partial current for H<sub>2</sub>O<sub>2</sub> generation than Pd black, and the mass activity per Pd of Pd-Se-B NC is 11-fold larger than that of Pd black at 0.6 V (vs. RHE) (Fig. S4c,d). Therefore, higher 2e<sup>-</sup> ORR activity of Pd-Se-B NC than metallic Pd is also verified in 1 × PBS electrolyte. However, it is noted that the H<sub>2</sub>O<sub>2</sub> selectivity of Pd-Se-B NC in 1 × PBS is lower than that in 0.1 M KPi (pH 8.0). The lower 2e<sup>-</sup> ORR selectivity in 1 × PBS could originate from (i) slightly lower pH and/or (ii) the presence of Cl<sup>-</sup>. To identify this, the electrochemical tests in 0.1 M KPi (pH 7.0) were performed (Fig. S5). In spite of lower onset potential of 0.65 V (vs. RHE), Pd-Se-B NC shows high H<sub>2</sub>O<sub>2</sub> selectivity of > 70% at pH 7.0 over the entire potential range investigated, which is similar to the results measured at pH 8.0 (Fig. S5a–c). Therefore, the lower H<sub>2</sub>O<sub>2</sub> selectivity in the PBS electrolyte can be ascribed in the presence of Cl<sup>-</sup>. Possible side reactions between Cl<sup>-</sup> and Pd-Se-B NC during the electrocatalysis can be neglected as evidenced by stable CV responses, which are similar to those measured in KPi electrolytes (Fig. S5d). It is assumed that Cl<sup>-</sup> in the PBS electrolyte affects the electric double layer structure, which in turn changes the reaction selectivity. The electrolyte effect requires more detailed investigation.

The 2e<sup>-</sup> ORR activities of Pd-Se-B NC in acidic and alkaline electrolytes were also investigated. Even under such extreme pH conditions (pH 0.3 and 13), the Pd-Se-B NC exhibited a significant H<sub>2</sub>O<sub>2</sub> selectivity, with a maximum value of 55% (Fig. S6). However, CV curves of Pd-Se-B

NC measured in the acidic and alkaline electrolytes changed markedly; the characteristic CV peaks corresponding to hydrogen underpotential deposition and PdO reduction gradually increased during successive potential cycles [51,52] (Fig. S7a,b). This is an indication of the presence of metallic Pd, implying that the Pd-Se-B NC underwent in situ surface transformation to metallic Pd phases during the CV in acidic and alkaline electrolytes. In contrast, the CV curves measured under neutral conditions exhibit negligible changes during the potential cycling (Fig. S7c).

### 3.3. Bulk electrolysis and stability test

To verify the sustained production of H<sub>2</sub>O<sub>2</sub>, Pd-Se-B NC was coated on carbon paper, and bulk electrolysis was performed in an H-cell. Electrolysis at fixed potentials (1 h at each) was performed at a range of potentials (0.2–0.55 V vs. RHE). The plot of the measured current density as a function of the applied potential indicated a similar potential-current density response compared with that obtained from the RRDE measurements (Figs. 3a, 4a, and S8). Iodometric titration of the electrolyte allowed for the quantification of the produced H<sub>2</sub>O<sub>2</sub> and subsequent calculation of Faradaic efficiency (FE) toward the H<sub>2</sub>O<sub>2</sub> production, after each electrolysis measurement (Fig. 4b). Pd-Se-B NC exhibited the H<sub>2</sub>O<sub>2</sub> FE values of > 70% over the entire potential range with the highest FE being 90 ± 3%. The stability of the Pd-Se-B NC during the reaction was confirmed by the XPS analysis of the catalyst-coated carbon paper before and after bulk electrolysis (Fig. 4c,d). The deconvoluted Pd and Se 3d XPS peak profiles changed negligibly, indicating the electrochemical stability of the Pd-Se-B NC under the reaction

conditions. The compositional stability was also demonstrated by the preserved relative surface atomic concentration of Pd to Se (Pd/Se) from 0.82 to 0.86 after the reaction. The slight increase in the relative Pd content could be explained by the removal of the quasi-stable partially oxidised  $\text{Se}^{6+}$  species during the electrochemical reactions as can be seen in the decrease of the corresponding XPS peaks in the Se 3d spectra (Fig. 4d).

#### 4. Conclusions

We synthesised a nanocoral-shaped Pd-based compound comprising mixed  $\text{Pd}_{17}\text{Se}_{15}$  and  $\text{Pd}_3\text{B}$  phases and demonstrated a marked difference in the reaction pathway for the ORR compared with the Pd metal catalyst. Pd-Se-B NC exhibited a high  $2e^-$  ORR activity and selectivity in near-neutral electrolytes, while Pd black catalysed the ORR almost entirely via the  $4e^-$  pathway. The  $2e^-$  ORR activity of the Pd-Se-B NC is one of the highest values in neutral media compared to those of previously reported electrocatalysts. Pd-Se-B NC also exhibited excellent stability during the electrochemical reactions. It is envisioned that the successful demonstration of Pd-Se-B NC for selective  $2e^-$  ORR will encourage the exploration of other compound compositions for  $2e^-$  ORR electrocatalysts in neutral or acidic media.

#### CRediT authorship contribution statement

**Juyeon Lee:** Validation, Data curation, Investigation, Writing – original draft. **Seung Woo Choi:** Validation, Data curation, Investigation, Writing – original draft. **Seoin Back:** Conceptualization, Writing – review & editing. **Hongje Jang:** Validation, Investigation, Writing – original draft, Writing – review & editing, Supervision, Funding acquisition. **Young Jin Sa:** Conceptualization, Validation, Investigation, Writing – original draft, Writing - review & editing, Supervision, Project administration, Funding acquisition.

#### Declaration of Competing Interest

There are no conflicts to declare.

#### Acknowledgements

This work was supported by the National Research Foundation (NRF) of Korea funded by Ministry of Science and ICT (NRF-2020R1C1C1006766, NRF-2019R1C1C1002305, and NRF-2021R1A6A1A03038785). The present research has been conducted by the Research Grant of Kwangwoon University in 2021.

#### Appendix A. Supporting information

Supplementary data associated with this article can be found in the online version at [doi:10.1016/j.apcatb.2022.121265](https://doi.org/10.1016/j.apcatb.2022.121265).

#### References

- [1] J.M. Campos-Martin, G. Blanco-Brieva, J.L.G. Fierro, Hydrogen peroxide synthesis: an outlook beyond the anthraquinone process, *Angew. Chem. Int. Ed.* 45 (2006) 6962–6984, <https://doi.org/10.1002/anie.200503779>.
- [2] Z. Chen, S. Chen, S. Siahrostami, P. Chakthranont, C. Hahn, D. Nordlund, S. Dimosthenis, J.K. Nørskov, Z. Bao, T. Jaramillo, Development of a reactor with carbon catalysts for modular-scale, low-cost electrochemical generation of  $\text{H}_2\text{O}_2$ , *React. Chem. Eng.* 2 (2017) 239–245, <https://doi.org/10.1039/C6RE00195E>.
- [3] S. Yang, A. Verdaguier-Casadevall, L. Amarson, L. Silvili, V. Čolić, R. Frydendal, J. Rossmeisl, I. Chorkendorff, I.E.L. Stephens, Toward the decentralized electrochemical production of  $\text{H}_2\text{O}_2$ : a focus on catalysis, *ACS Catal.* 8 (2018) 4064–4081, <https://doi.org/10.1021/acscatal.8b00217>.
- [4] J. Gao, B. Liu, Progress of electrochemical hydrogen peroxide synthesis over single atom catalysts, *ACS Mater. Lett.* 2 (2020) 1008–1024, <https://doi.org/10.1021/acsmaterialslett.0c00189>.
- [5] S. Siahrostami, S.J. Villegas, A.H.B. Mostaghimi, S. Back, A.B. Farimani, H. Wang, K.A. Persson, J. Montoya, A review on challenges and successes in atomic-scale design of catalysts for electrochemical synthesis of hydrogen peroxide, *ACS Catal.* 10 (2020) 7495–7511, <https://doi.org/10.1021/acscatal.0c01641>.
- [6] K. Jiang, J. Zhao, H. Wang, Catalyst design for electrochemical oxygen reduction toward hydrogen peroxide, *Adv. Funct. Mater.* 30 (2020), 2003321, <https://doi.org/10.1002/adfm.202003321>.
- [7] J.S. Jirkovský, I. Panas, E. Ahlberg, M. Halasa, S. Romani, D.J. Schiffrin, Single atom hot-spots at Au–Pd nanoalloys for electrocatalytic  $\text{H}_2\text{O}_2$  production, *J. Am. Chem. Soc.* 133 (2011) 19432–19441, <https://doi.org/10.1021/ja206477z>.
- [8] S. Siahrostami, A. Verdaguier-Casadevall, M. Karamad, D. Deiana, P. Malacrida, B. Wickman, M. Escudero-Escribano, E.A. Paoli, R. Frydendal, T.W. Hansen, I. Chorkendorff, I.E.L. Stephens, J. Rossmeisl, Enabling direct  $\text{H}_2\text{O}_2$  production through rational electrocatalyst design, *Nat. Mater.* 12 (2013) 1137–1143, <https://doi.org/10.1038/nmat3795>.
- [9] A. Verdaguier-Casadevall, D. Deiana, M. Karamad, S. Siahrostami, P. Malacrida, T.W. Hansen, J. Rossmeisl, I. Chorkendorff, I.E.L. Stephens, Trends in the electrochemical synthesis of  $\text{H}_2\text{O}_2$ : enhancing activity and selectivity by electrocatalytic site engineering, *Nano Lett.* 14 (2014) 1603–1608, <https://doi.org/10.1021/nl500037x>.
- [10] Z. Zheng, Y.H. Ng, D.-W. Wang, R. Amal, Epitaxial growth of Au–Pt–Ni nanorods for direct high selectivity  $\text{H}_2\text{O}_2$  production, *Adv. Mater.* 28 (2016) 9949–9955, <https://doi.org/10.1002/adma.201603662>.
- [11] E. Pizzutillo, S.J. Freakley, S. Cherevko, S. Venkatesan, G.J. Hutchings, C. H. Liebscher, G. Dehm, K.J.J. Mayrhofer, Gold–Palladium bimetallic catalyst stability: consequences for hydrogen peroxide selectivity, *ACS Catal.* 7 (2017) 5699–5705, <https://doi.org/10.1021/acscatal.7b01447>.
- [12] K. Cao, H. Yang, S. Bai, Y. Xu, C. Yang, Y. Wu, M. Xie, T. Cheng, Q. Shao, X. Huang, Efficient direct  $\text{H}_2\text{O}_2$  synthesis enabled by PdPb nanorings via inhibiting the O–O bond cleavage in  $\text{O}_2$  and  $\text{H}_2\text{O}_2$ , *ACS Catal.* 11 (2021) 1106–1118, <https://doi.org/10.1021/acscatal.0c04348>.
- [13] S. Back, J. Na, Z.W. Ulissi, Efficient discovery of active, selective, and stable catalysts for electrochemical  $\text{H}_2\text{O}_2$  synthesis through active motif screening, *ACS Catal.* 11 (2021) 2483–2491, <https://doi.org/10.1021/acscatal.0c05494>.
- [14] C.H. Choi, H.C. Kwon, S. Yook, H. Shin, H. Kim, M. Choi, Hydrogen peroxide synthesis via enhanced two-electron oxygen reduction pathway on carbon-coated Pt surface, *J. Phys. Chem. C* 118 (2014) 30063–30070, <https://doi.org/10.1021/jp5113894>.
- [15] C.H. Choi, M. Kim, H.C. Kwon, S.J. Cho, S. Yun, H.-T. Kim, K.J.J. Mayrhofer, H. Kim, M. Choi, Tuning selectivity of electrochemical reactions by atomically dispersed platinum catalyst, *Nat. Commun.* 7 (2016) 10922, <https://doi.org/10.1038/ncomms10922>.
- [16] S. Yang, J. Kim, Y.J. Tak, A. Soon, H. Lee, Single-atom catalyst of platinum supported on titanium nitride for selective electrochemical reactions, *Angew. Chem. Int. Ed.* 55 (2016) 2058–2062, <https://doi.org/10.1002/anie.201509241>.
- [17] R. Shen, W. Chen, Q. Peng, S. Lu, L. Zheng, X. Cao, Y. Wang, W. Zhu, J. Zhang, Z. Zhuang, C. Chen, D. Wang, Y. Li, High-concentration single atomic Pt sites on hollow  $\text{CuS}_2$  for selective  $\text{O}_2$  reduction to  $\text{H}_2\text{O}_2$  in acid solution, *Chem* 5 (2019) 2099–2110, <https://doi.org/10.1016/j.chempr.2019.04.024>.
- [18] J.H. Kim, D. Shin, J. Lee, D.S. Baek, T.J. Shin, Y.-T. Kim, H.Y. Jeong, J.H. Kwak, H. Kim, S.H. Joo, A general strategy to atomically dispersed precious metal catalysts for unravelling their catalytic trends for oxygen reduction reaction, *ACS Nano* 14 (2020) 1990–2001, <https://doi.org/10.1021/acsnano.9b08494>.
- [19] J.H. Kim, D. Shin, J. Kim, J.S. Lim, V.K. Paidi, T.J. Shin, H.Y. Jeong, K.-S. Lee, H. Kim, S.H. Joo, Reversible ligand exchange in atomically dispersed catalysts for modulating the activity and selectivity of the oxygen reduction reaction, *Angew. Chem. Int. Ed.* 60 (2021) 20528–20534, <https://doi.org/10.1002/anie.202108439>.
- [20] Y. Wang, Y. Wang, J. Zhao, Y. Xu, Effect of inorganic ions on  $\text{H}_2\text{O}_2$  production over illuminated Au/ $\text{WO}_3$  with visible light, *Appl. Catal. B* 299 (2021), 120676, <https://doi.org/10.1016/j.apcatb.2021.120676>.
- [21] H. Sheng, E.D. Hermes, X. Yang, D. Ying, A.N. Janes, W. Li, J.R. Schmidt, S. Jin, Electrocatalytic production of  $\text{H}_2\text{O}_2$  by selective oxygen reduction using earth-abundant cobalt pyrite ( $\text{CoS}_2$ ), *ACS Catal.* 9 (2019) 8433–8442, <https://doi.org/10.1021/acscatal.9b02546>.
- [22] F. Ma, S. Wang, X. Liang, C. Wang, F. Tong, Z. Wang, P. Wang, Y. Liu, Y. Dai, Z. Zheng, B. Huang,  $\text{Ni}_3\text{B}$  as a highly efficient and selective catalyst for the electrosynthesis of hydrogen peroxide, *Appl. Catal. B* 279 (2020), 119371, <https://doi.org/10.1016/j.apcatb.2020.119371>.
- [23] E. Jung, H. Shin, B.-H. Lee, V. Efremov, S. Lee, H.S. Lee, J. Kim, W.H. Antink, S. Park, K.-S. Lee, S.-P. Cho, J.S. Yoo, Y.-S. Sung, T. Hyeon, Atomic-level tuning Co–N–C catalysts for high-performance electrochemical  $\text{H}_2\text{O}_2$  production, *Nat. Mater.* 19 (2020) 436–442, <https://doi.org/10.1038/s41563-019-0571-5>.
- [24] K. Jiang, S. Back, A.J. Akey, C. Xia, Y. Hu, W. Liang, D. Schaak, E. Stavitski, J. K. Nørskov, S. Siahrostami, H. Wang, Highly selective reduction to hydrogen peroxide on transition metal single atom coordination, *Nat. Commun.* 10 (2019) 3997, <https://doi.org/10.1038/s41467-019-11992-2>.
- [25] C. Tang, Y. Jiao, B. Shi, J.-N. Liu, Z. Xie, X. Chen, Q. Zhang, S.-Z. Qiao, Coordination tunes selectivity: Two-electron oxygen reduction on high-loading molybdenum single-atom catalysts, *Angew. Chem. Int. Ed.* 59 (2020) 9171–9176, <https://doi.org/10.1002/anie.202003842>.
- [26] C. Liu, H. Li, F. Liu, J. Chen, Z. Yu, Z. Yuan, C. Wang, H. Zheng, G. Henkelman, L. Wei, Y. Chen, Intrinsic activity of metal centers in metal–nitrogen–carbon single-atom catalysts for hydrogen peroxide synthesis, *J. Am. Chem. Soc.* 142 (2020) 21861–21871, <https://doi.org/10.1021/jacs.0c10636>.
- [27] Y. Zheng, X. Xu, J. Chen, Q. Wang, Surface  $\text{O}^{2-}$  regulation on POM electrocatalyst to achieve accurate  $2e^-/4e^-$  ORR control for  $\text{H}_2\text{O}_2$  production and Zn-air battery assemble, *Appl. Catal. B* 285 (2021), 119788, <https://doi.org/10.1016/j.apcatb.2020.119788>.

- [28] Y.-P. Chen, S.-Y. Lin, R.-M. Sun, A.-J. Wang, L. Zhang, X. Ma, J.-J. Feng, FeCo/FeCoP encapsulated in N, Mn-codoped three-dimensional fluffy porous carbon nanostructures as highly efficient bifunctional electrocatalyst with multi-components synergistic catalysis for ultra-stable rechargeable Zn-air batteries, *J. Colloid Interface Sci.* 605 (2022) 451–462, <https://doi.org/10.1016/j.jcis.2021.07.082>.
- [29] R.-M. Sun, L. Zhang, J.-J. Feng, K.-M. Fang, A.-J. Wang, *In situ* produced Co9S8 nanoclusters/Co/Mn-S,N multi-doped 3D porous carbon derived from eriochrome black T as an effective bifunctional oxygen electrocatalyst for rechargeable Zn-air batteries, *J. Colloid Interface Sci.* 608 (2022) 2100–2110, <https://doi.org/10.1016/j.jcis.2021.10.144>.
- [30] Z. Lu, G. Chen, S. Siahrostami, Z. Chen, K. Liu, J. Xie, L. Liao, T. Wu, D. Lin, Y. Liu, Thomas F. Jaramillo, J.K. Nørskov, Y. Cui, High-efficiency oxygen reduction to hydrogen peroxide catalysed by oxidized carbon materials, *Nat. Catal.* 1 (2018) 156–162, <https://doi.org/10.1038/s41929-017-0017-x>.
- [31] H.Y. Kim, M.B. Ross, N. Kornienko, L. Zhang, J. Guo, P. Yang, B.D. McCloskey, Efficient hydrogen peroxide generation using reduced graphene oxide-based oxygen reduction electrocatalysts, *Nat. Catal.* 1 (2018) 282–290, <https://doi.org/10.1038/s41929-018-0044-2>.
- [32] S. Chen, Z. Chen, S. Siahrostami, D. Higgins, D. Nordlund, D. Sokaras, T.R. Kim, Y. Liu, X. Yan, E. Nilsson, R. Sinclair, J.K. Nørskov, T.F. Jaramillo, Z. Bao, Designing boron nitride islands in carbon materials for efficient electrochemical synthesis of hydrogen peroxide, *J. Am. Chem. Soc.* 140 (2018) 7851–7859, <https://doi.org/10.1021/jacs.8b02798>.
- [33] Y. Sun, I. Sinev, W. Ju, A. Bergmann, S. Dresch, S. Kühn, C. Spöri, H. Schmies, H. Wang, D. Bernsmeier, B. Paul, R. Schmack, R. Kraehnert, B.R. Cuenya, P. Strasser, Efficient electrochemical hydrogen peroxide production from molecular oxygen on nitrogen-doped mesoporous carbon catalysts, *ACS Catal.* 8 (2018) 2844–2856, <https://doi.org/10.1021/acscatal.7b03464>.
- [34] Y.J. Sa, J.H. Kim, S.H. Joo, Active edge-site-rich carbon nanocatalysts with enhanced electron transfer for efficient electrochemical hydrogen peroxide production, *Angew. Chem. Int. Ed.* 58 (2019) 1100–1105, <https://doi.org/10.1002/anie.201812435>.
- [35] G.-F. Han, F. Li, W. Zou, M. Karamad, J.-P. Jeon, S.-W. Kim, S.-J. Kim, Y. Bu, Z. Fu, Y. Lu, S. Siahrostami, J.-B. Baek, Building and identifying highly active oxygenated groups in carbon materials for oxygen reduction to H<sub>2</sub>O<sub>2</sub>, *Nat. Commun.* 11 (2020) 2209, <https://doi.org/10.1038/s41467-020-15782-z>.
- [36] K.-H. Wu, D. Wang, X. Lu, X. Zhang, Z. Xie, Y. Liu, B.-J. Su, J.-M. Chen, D.-S. Su, W. Qi, S. Guo, Highly selective hydrogen peroxide electrosynthesis on carbon: *In situ* interface engineering with surfactants, *Chem* 6 (2020) 1443–1458, <https://doi.org/10.1016/j.chempr.2020.04.002>.
- [37] Z. Wang, Q.-K. Li, C. Zhang, Z. Cheng, W. Chen, E.A. McHugh, R.A. Carter, B. I. Yakobson, J.M. Tour, Hydrogen peroxide generation with 100% faradaic efficiency on metal-free carbon black, *ACS Catal.* 11 (2021) 2454–2459, <https://doi.org/10.1021/acscatal.0c04735>.
- [38] F. Sun, C. Yang, Z. Qu, W. Zhou, Y. Ding, J. Gao, G. Zhao, D. Xing, Y. Lu, Inexpensive activated coke electrocatalyst for high-efficiency hydrogen peroxide production: Coupling effects of amorphous carbon cluster and oxygen dopant, *Appl. Catal. B* 286 (2021), 119860, <https://doi.org/10.1016/j.apcatb.2020.119860>.
- [39] J.S. Lim, J.H. Kim, J. Woo, D.S. Baek, K. Ihm, T.J. Shin, Y.J. Sa, S.H. Joo, Designing highly active nanoporous carbon H<sub>2</sub>O<sub>2</sub> production electrocatalysts through active site identification, *Chem* 7 (2021) 1–17, <https://doi.org/10.1016/j.chempr.2021.08.007>.
- [40] M. Beck, M. Ellner, E.J. Mittemeijer, Powder diffraction data for borides Pd<sub>3</sub>B and Pd<sub>5</sub>B<sub>2</sub> and the formation of an amorphous boride Pd<sub>2</sub>B, *Powder Diff.* 16 (2001) 98–101, <https://doi.org/10.1154/1.1351156>.
- [41] E. Desimoni, G.I. Casella, T.R.I. Cataldi, C. Malatesta, A comparison of some asymmetrical line shapes for XPS data analysis, *J. Electron Spectrosc. Relat. Phenom.* 49 (1989) 247–261, [https://doi.org/10.1016/0368-2048\(89\)85012-1](https://doi.org/10.1016/0368-2048(89)85012-1).
- [42] S. Kaur, G. Mera, R. Riedel, E. Ionescu, Effect of boron incorporation on the phase composition and high-temperature behavior of polymer-derived silicon carbide, *J. Eur. Ceram. Soc.* 36 (2016) 967–977, <https://doi.org/10.1016/j.jeurceramsoc.2015.11.037>.
- [43] L. Liang, M. Zhou, X. Lu, P. Su, J. Sun, High-efficiency electrogeneration of hydrogen peroxide from oxygen reduction by carbon xerogels derived from glucose, *Electrochim. Acta* 320 (2019), 134569, <https://doi.org/10.1016/j.electacta.2019.134569>.
- [44] H. Zhang, Y. Li, Y. Zhao, G. Li, F. Zhang, Carbon black oxidized by air calcination for enhanced H<sub>2</sub>O<sub>2</sub> generation and effective organics degradation, *ACS Appl. Mater. Interfaces* 11 (2019) 27846–27853, <https://doi.org/10.1021/acsami.9b07765>.
- [45] P.T. Smith, Y. Kim, B.P. Benke, K. Kim, C.J. Chang, Supramolecular tuning enables selective oxygen reduction catalyzed by cobalt porphyrins for direct electrosynthesis of hydrogen peroxide, *Angew. Chem. Int. Ed.* 59 (2020) 4902–4907, <https://doi.org/10.1002/anie.201916131>.
- [46] N. Wang, S. Ma, J. Duan, X. Zhai, F. Guan, X. Wang, B. Hou, Electrocatalytic oxygen reduction to hydrogen peroxide by oxidized graphene aerogel supported cubic MnCO<sub>3</sub> for antibacteria in neutral media, *Electrochim. Acta* 340 (2020), 135880, <https://doi.org/10.1016/j.electacta.2020.135880>.
- [47] Y. Pang, K. Wang, H. Xie, Y. Sun, M.-M. Titirici, G.-L. Chai, Mesoporous carbon hollow spheres as efficient electrocatalysts for oxygen reduction to hydrogen peroxide in neutral electrolytes, *ACS Catal.* 10 (2020) 7434–7442, <https://doi.org/10.1021/acscatal.0c00584>.
- [48] P. Su, M. Zhou, G. Song, X. Du, X. Lu, Efficient H<sub>2</sub>O<sub>2</sub> generation and spontaneous-OH conversion for in-situ phenol degradation on nitrogen-doped graphene: pyrolysis temperature regulation and catalyst regeneration mechanism, *J. Hazard. Mater.* 397 (2020), 122681, <https://doi.org/10.1016/j.jhazmat.2020.122681>.
- [49] R. Hu, Y. Cui, B. Huang, L. Guan, Transforming C<sub>60</sub> molecules into polyhedral carbon micro-nano shells for electrochemically producing H<sub>2</sub>O<sub>2</sub> in neutral electrolytes, *ACS Appl. Mater. Interfaces* 13 (2021) 35856–35864, <https://doi.org/10.1021/acsami.1c11318>.
- [50] B. Huang, Y. Cui, R. Hu, J. Huang, L. Guan, Promoting the two-electron oxygen reduction reaction performance of carbon nanospheres by pore engineering, *ACS Appl. Energy Mater.* 4 (2021) 4620–4629, <https://doi.org/10.1021/acsaem.1c00259>.
- [51] S. Hu, F. Munoz, J. Noborikawa, H. Haan, L. Scudiero, S. Ha, Carbon supported Pd-based bimetallic and trimetallic catalyst for formic acid electrochemical oxidation, *Appl. Catal. B* 180 (2016) 758–765, <https://doi.org/10.1016/j.apcatb.2015.07.023>.
- [52] Z.X. Liang, T.S. Zhao, J.B. Xu, L.D. Zhu, Mechanism study of the ethanol oxidation reaction on palladium in alkaline media, *Electrochim. Acta* 54 (2009) 2203–2208, <https://doi.org/10.1016/j.electacta.2008.10.034>.